Effective Photocatalytic H_2O_2 Production under Visible Light Irradiation at g-C_3N_4 Modulated by Carbon Vacancies

Shuna Li [a,b], Guohui Dong [a,*], Reshalaiti Hailili [a], Liping Yang [a], Yingxuan Li [a], Fu Wang [a], Yubin Zeng [b,*], and Chuanyi Wang [a,b,*]

a Laboratory of Environmental Sciences and Technology, Xinjiang Technical Institute of Physics & Chemistry; Key Laboratory of Functional Materials and Devices for Special Environments, Chinese Academy of Sciences, Urumqi 830011, China

b School of Power and Mechanical Engineering, Wuhan university, hubei 430072, China

[*]*Corresponding author.* Phone: +86-991-3835879; Fax: +86-991-3838957.

Email address: donggh@ms.xjb.ac.cn; zengyubin@whu.edu.cn; cywang@ms.xjb.ac.cn.

Abstract

Hydrogen peroxide (H_2O_2) is of great significance in biological and environmental processes as well as in chemical industry. Even though anthraquinone autoxidation (AO) process has been the major artificial way to produce H_2O_2, its energy cost and non-green nature have been motivating people to develop more efficient, economical and green technologies as alternatives. Here we demonstrated that photocatalytic

H_2O_2 production at g-C_3N_4 could be improved by as much as 14 times in the absence of organic scavenger through a carbon vacancy-based strategy. Both the experimental and theoretical calculation results indicated that the creation of carbon vacancies could reduce the symmetry of g-C_3N_4 and produce the effect of electron delocalization. This will allow g-C_3N_4 to possess more excitable electrons and a narrower band gap. On the other hand, carbon vacancies provided more sites to adsorb molecular oxygen and thereby help electrons transfer from g-C_3N_4 to the surface adsorbed O_2. More interestingly, the presence of carbon vacancies changed the H_2O_2 generation pathway from a two-step single-electron indirect reduction to an one-step two-electron direct reduction. This study could not only develop a novel strategy to improve the H_2O_2 production activity of semiconductors, but also shed light on the deep understanding of the role played by surface defect structure on photocatalytic activity of semiconductor photocatalysts.

Key words: Photocatalysis, hydrogen peroxide, carbon vacancy, g-C_3N_4, oxygen reduction

1. Introduction

Hydrogen peroxide (H_2O_2) is an extremely versatile and useful agent. It is widely used in biological process, environmental remediation and chemical industry [1-3]. In the field of environmental remediation, H_2O_2 is a potent oxidant, which can directly or indirectly (in combination with other technology) oxidize a variety of organic or inorganic pollutants [4-6]. Since its reaction products are H_2O and O_2 only, H_2O_2 can also serve as an environmentally safe oxidant with numerous industrial applications

including chemical syntheses, paper bleaching, textile bleaching and detergents production [7-10]. At present, the main methods for large-scale production of H_2O_2 include anthraquinone autoxidation, oxidation of alcohols and electrochemical synthesis [11-13]. However, these methods can hardly be considered as green ones due to the consumption of a large amount of energy or organic solvent. In addition, H_2O_2 extracted from these systems may be contaminated by organic impurities. Therefore, it is highly desirable to develop efficient, economical and green technologies for the production of H_2O_2.

Recently, H_2O_2 production from semiconductor photocatalytic process has attracted much attention because this procedure uses the sufficient and renewable sunlight as the driving force. Moreover, the photocatalytic approach does not need to use H_2 and can be a safe and green method. In the past decades, the H_2O_2 production photocatalysts were mainly focused on TiO_2 and modified TiO_2 [14-16]. For example, Maurino *et al*. reported that surface fluorination of TiO_2 could lead to an increase in the production rate of H_2O_2 [14]. Tsukamoto *et al*. found that the surface deposition with Au-Ag alloy could improve the H_2O_2 production rate of TiO_2 [16]. Although TiO_2 or modified TiO_2 in the presence of oxygen can effectively produce H_2O_2 under UV light irradiation, H_2O_2 also suffer self-decomposition induced by UV light [17]. Furthermore, UV light accounts for only ~4% of sunlight [18]. Therefore, it is essential to design and develop visible light active photocatalysts which could efficiently produce H_2O_2 while inhibit the decomposition process.

Graphitic carbon nitride (g-C_3N_4) is a metal-free visible light photocatalyst very

promising for hydrogen evolution because of its desirable band gap of 2.7 eV [19-21]. Since its conduction band potential (-1.3 V) is more negative than the reduction potential of O_2/H_2O_2 (0.695 V), g-C_3N_4 could reduce O_2 to H_2O_2 under visible light thermodynamically [22, 23]. Shiraishi *et al*. found that H_2O_2 could be effectively produced by g-C_3N_4 in water/alcohol mixture under visible light irradiation [24]. However, in the absence of alcohol (organic scavenger), the efficacy of pure g-C_3N_4 was very low [25, 26]. This is due to the fact that pure g-C_3N_4 has two disadvantages: (1) the fast recombination of photogenerated electrons and holes; (2) low chemical adsorption capability of O_2 on its surface [27-29]. According to previous reports, vacancy defects have been found to be able to trap photogenerated electrons thus inhibiting the recombination of photogenerated electrons and holes [30-32]. Meanwhile, vacancy defects can also enhance the adsorption and activation of gas molecular because of their abundant localized electrons [33, 34]. In addition, amino nitrogen components can remarkably promote the interfacial electron transfer as recently observed by Zhang and his coworkers [35]. Considering the advantages of vacancy and amino nitrogen, it is reasonable to hypothesize that the coexistence of vacancy defects and amino nitrogen may improve the H_2O_2 production activity of g-C_3N_4 in absence of organic scavenger. Coincidentally, the formation of carbon vacancies in the structure of g-C_3N_4 is accompanied by the appearance of amino group (Scheme 1). Therefore, it is of great interest to systematically study the correlation between carbon vacancy and H_2O_2 production performance of g-C_3N_4. However, to the best of our knowledge, limited work has been presented in this

regard.

In this study, the effects of carbon vacancies on the oxygen reduction over g-C_3N_4 and the generation of H_2O_2 were systematically explored. Experimental results showed that carbon vacancy greatly improved the activity of g-C_3N_4 for H_2O_2 production in the absence of organic scavenger. A series of experiments were designed to identify the roles of carbon vacancies on the H_2O_2 production of g-C_3N_4 under visible light, and the mechanisms for the enhanced activity were analyzed in detail.

2. Experiments

2.1 Sample Preparation. g-C_3N_4 was synthesized by following the protocol developed in our previous work [36]. Melamine (4 g) in a covered crucible (30 mL) was heated in static air with a ramp rate of 20 °C/min up to 520 °C where it was held for 4 h. Carbon vacancy contained g-C_3N_4 (Cv-g-C_3N_4) was synthesized by calcining the as-prepared g-C_3N_4 in a tube furnace at 520 °C under high purity argon gas flow for 2 h. The resulted agglomerates were milled into powder in an agate mortar for further use.

2.2 Characterization. Power X-ray diffraction (XRD) patterns of the resulted samples were recorded on a Bruker D8 Advance diffractometer using Cu K_α irradiation (λ = 1.5418 Å). Element analysis was performed on Vario MICRO. Fourier transform infrared (FT-IR) spectra were obtained on an FT-IR spectrophotometer (Nicolet iS50, Thermo) with KBr as the reference. Chemical compositions of the samples were analyzed using X-ray photoelectronspectroscopy (XPS) (VG Scientific ESCALAB Mark II spectrometer equipped with two ultrahigh vacuum chambers). All

the binding energies were calibrated to the C 1s peak (284.6 eV) arising from the adventitious carbon. Electron spin resonance (ESR) signals were recorded on a Bruker ESR A300 spectrometer at room temperature (298 K). The Brunauer-Emmett-Teller surface areas of the samples were determined by nitrogen adsorption-desorption isotherm measurements at 77 K, using a Micrometrics ASAP2020 system after samples were vacuum-dried at 180 °C overnight. Optical absorption spectra were obtained using a UV-visible spectrometer (Shimadzu UV-2550). Photoluminescence spectra (PL) were measured on a fluorescence spectrometer (Hitachi F-4500) at 293 K.

2.3 Photocatalytic experiments. The photocatalytic activities of the samples were evaluated by the activation of molecular oxygen under visible light irradiation ($\lambda >$ 420 nm). A 300 W Xenon lamp with a 420 nm cutoff filter was chosen as visible light source. During each photocatalytic experiment, 0.1 g of a photocatalyst sample was dispersed into 100 mL of distilled water in a container with cooling water jacket outside. After that, the photocatalyst dispersion system was stirred in the dark for 2 h to ensure the adsorption-desorption equilibrium among the photocatalyst, dissolved oxygen and water before visible light irradiation. During the irradiation, about 4 mL of the suspensions was taken from the reaction cell at given time intervals, and then centrifuged to remove the photocatalyst particles. Subsequently, hydrogen peroxide (H_2O_2) was measured using a (p-hydroxyphenyl) acetic acid (POHPAA) analysis method [37]. Typically, a certain volume of fluorescence reagent (potassium hydrogen phthalate: 8.2 g/L, p-hydroxyphenylacetic acid: 270 mg/L, and type II horseradish

peroxidase: 30 mg/L) was pre-added into the reaction system. 1.0 mL of sample was then withdrawn at an interval time of 2 h and then mixed with 1.0 mL of 1.0 mol/L NaOH for 10 min for measuring the intensity of the fluorescence emission at 409 nm excited at 315 nm.

Superoxide radicals ($\cdot O_2^-$) were examined by electron spin resonance (ESR) spectral measurement. ESR spectra of the radicals were recorded on a Bruker EPR A300 spectrometer employing 5,5-dimethyl-l-pyrroline-N-oxide (DMPO) as the spin trapper. The spectra were collected with averages of 9 scans at 2 min after mixing the test sample in methanol solution. Methanol was used as the ·OH radical scavenger to suppress the DMPO-OH signal.

2.4 Theoretical calculations. The band structures and electron density calculations were carried out using the program package CASTEP, working in a plane wave basis set. The Brillouin zones of the supercells were sampled by a grid of 3 × 3 × 1 (g-C_3N_4 and Cv-g-C_3N_4) K-points. Electronic structures were calculated within the generalized gradient approximation from Perdew-Burke-Ernzerhof (GGA-PBE). The cutoff energy was 550 eV, and the Monkhorst-Pack k-point meshes were 5×5×3 for all structures. In the process of calculation, the convergence tolerances were set as follows: 2.72e-5 eV/ atom for energy, 0.002 eV/ Å for maximal force, 0.05 GPa for maximal stress, and 0.001 Å for max.

2.5 Photoelectrochemical experiments. Photoelectrochemical experiments were performed in a conventional three-electrode cell with a platinum plate (1×1 cm^2) as the auxiliary electrode and a saturated calomel electrode (SCE) as the reference

electrode on a CHI 660C workstation. The photoelectrode (working electrode) was positioned in the middle of a 0.1 M KCl aqueous solution with the glass side facing the incident light. A 300W Xe lamp with a 420 nm cutoff filter was chosen as a visible light source.

The photoelectrodes were prepared by a spin coating method. Typically, the aqueous slurries of g-C_3N_4 and Cv-g-C_3N_4 were spin-coated on ITO glass substrate at a spin rate of 3000 rpm for 30 s under low vacuum. The films on ITO glass substrate were dried in air and annealed at 200 ^oC for 1 h as final photoelectrodes.

3. Results and Discussion

3.1 Structure Characterization for Samples. X-ray diffraction (XRD) is often used to characterize the phase structure of samples. As well known, g-C_3N_4 is featured with two XRD peaks: one at 13.0^o corresponding to a d-spacing of 0.676 nm is arising from the in-plane structural packing motif, and the other at 27.4^o is a characteristic interlayer stacking peak, corresponding to an interlayer distance of d=0.336 nm. As shown in Figure 1a, both samples show a typical g-C_3N_4 structure without any impurity phases, indicating that the heat treatment with argon gas did not affect the crystal structure of graphite-like carbon nitride. However, the peaks of Cv-g-C_3N_4 are weaker and shifted toward a higher 2θ value, suggesting that heat treatment with argon gas could destroy the crystallinity of g-C_3N_4 and could produce defects.

In order to identify the type of defects formed in the Cv-g-C_3N_4 framework, elemental analysis (EA) was used to determine the molar ratio of carbon to nitrogen (C/N) in the products. The C/N molar ratio of Cv-g-C_3N_4 is 0.6 (Figure 1b), lower

than that of g-C_3N_4 (0.7). This indicates that the defects formed in the Cv-g-C_3N_4 framework are carbon vacancies. Additionally, the content of H element in Cv-g-C_3N_4 is very plentiful, suggesting that more amino groups (-NH_2) were generated in Cv-g-C_3N_4 after the heat treatment with argon gas.

X-ray photoelectron spectroscopy (XPS) was further used to investigate the chemical compositions of the carbon nitride samples (Figures 2a and 2b). High-resolution XPS peaks of C 1*s* of the two samples can be fitted with two peaks at binding energies of 288.2 and 284.6 eV, which are ascribed to the tertiary carbon C-N_3 and C-C (arising from the adventitious carbon) groups, respectively. The area ratios of the two peaks at 288.2 and 284.6 eV were calculated to be 2.7 and 1.2 for g-C_3N_4 and Cv-g-C_3N_4, respectively. The decrease of tertiary carbon content percentage supports the assumption of carbon vacancy formation. In addition, the high-resolution XPS peaks of N 1*s* of g-C_3N_4 can be fitted with two peaks centered at 398.4 and 400.7 eV, which are ascribed to the tertiary carbon C-N-C and C-N_3 (arising from the adventitious carbon) groups, respectively. However, in addition to the N 1*s* peaks at 398.4 and 400.7 eV, a new peak at higher binding energy of 401.3 eV appeared in the high-resolution XPS spectra of Cv-g-C_3N_4 (Figure 2b). This peak is attributed to the amino groups (-NH_2) formed by the disappearance of tertiary carbon and further supports the formation of carbon vacancies.

Besides EA and XPS, Electron spin resonance (ESR) was also employed to verify the formation of carbon vacancies. Figure 2c shows that g-C_3N_4 exhibits a Lorentzian line centered at about 3512 G, which is arisen from the unpaired electrons on the

carbon atoms of the aromatic rings. Compare with pure g-C_3N_4, Cv-g-C_3N_4 possesses a much weaker ESR signal, suggesting the decrease of carbon content in Cv-g-C_3N_4. Therefore, it is concluded that carbon vacancies have been successfully formed in g-C_3N_4 after the heat treatment with argon gas.

Since surface and bulk defects play different roles in photocatalytic processes, it is crucial to identify the positions of carbon vacancies in the Cv-g-C_3N_4. In this prospect, high-resolution XPS depth profiles analysis was employed to monitor the -NH_2 change in the Cv-g-C_3N_4. It is found that the peak intensity of -NH_2 decreases continuously upon the etching time from 0 to 240 s, indicating the carbon vacancies mainly exist on the surface of Cv-g-C_3N_4 (Figure S1, in the supporting information). Figure 2d shows the possible formation mechanism of carbon vacancy. In the procedure of calcination, high temperature give the enormous energy to argon molecules. This makes a part of argon molecules do the irregular motion. Molecules which do irregular motion may hit the surface atoms. When argon molecule hit surface atom, it will impart energy to the targeted atom. If the imparted energy exceeds the binding energy of the targeted atom, targeted atom can be sputtered from the surface and form a vacancy simultaneously. As we know, carbon atom has a bigger surface area and smaller molecular weight than nitrogen atom. The bigger surface area makes carbon atom to accept more energy. Meanwhile, the smaller molecular weight and the bigger energy make carbon atom more likely to be sputtered from the surface.

3.2 Photocatalytic H_2O_2 production. H_2O_2 can be produced in both g-C_3N_4 and Cv-g-C_3N_4 systems (Figure 3). Control experiments show that H_2O_2 cannot be detected when oxygen is eliminated by argon gas, indicating oxygen is essential for the generation of H_2O_2 (Figure 3a). That means O_2 could be effectively reduced to H_2O_2 in the presence of water over both g-C_3N_4 and Cv-g-C_3N_4. However, in the absence of either photocatalyst or visible light, there is no H_2O_2 production (Figure 3a). This result unambiguously illustrates that the process of H_2O_2 production is accomplished by photocatalysis (Figure 3c). As shown in Figures 3a and 3d, the H_2O_2 production in g-C_3N_4 suspension slowly increases with extending the reaction time. Interestingly, the yield of produced H_2O_2 over Cv-g-C_3N_4 in the same visible light irradiation time is much higher than that over g-C_3N_4 (Figures 3b and 3d). Obviously, Cv-g-C_3N_4 is more active for the photoreduction of O_2 to H_2O_2, namely, 14 times more activity than g-C_3N_4. The influence of initial pH values on the H_2O_2 generation in the Cv-g-C_3N_4/H_2O/O_2 system was also investigated. We found that the pH value variation in the range of 5.0 to 7.0 did not affect the H_2O_2 production (Figure S2, in the supporting information), suggesting that Cv-g-C_3N_4 can efficiently produce H_2O_2 in a wide working pH range.

Niu and her co-workers revealed that nitrogen vacancy could also improve the photocatalytic activity of g-C_3N_4 [38]. To compare the improve effect of carbon vacancy and nitrogen vacancy, we synthesized the g-C_3N_4 with nitrogen vacancies (Nv-g-C_3N_4). The synthesis procedure of Nv-g-C_3N_4 was similar to that of Cv-g-C_3N_4 but changed the argon gas to hydrogen gas. The activity comparison in Figure S3 (In

supporting information) suggests that the activity of Cv-g-C_3N_4 is 6 times of that of Nv-g-C_3N_4. This result suggests that carbon vacancy is more effective for photocatalytic H_2O_2 generation than nitrogen vacancy.

3.3 The mechanism of activity enhancement. Since the production of H_2O_2 needs photogenerated electrons to reduce O_2, the generation of H_2O_2 relies on the amount of photogenerated electrons. As is well known, photocurrent also depends on the amount of photoelectrons transferred from semiconductor to the ITO glass substrate. The higher the photocurrent is, the more the photoelectrons are produced. Figure 4a shows that the photocurrent (The applied bias is 0 V vs SCE) generated over Cv-g-C_3N_4 reaches 8.12 μA cm^{-2}, 2.0 times that of g-C_3N_4 (4.05 μA cm^{-2}). The higher photocurrent in Cv-g-C_3N_4 implies that it could produce more photoelectrons to reduce O_2 molecule compared to g-C_3N_4.

Generally, the production of photoelectrons relates to three processes: visible light absorption, photoexcitation, and the separation of photoinduced charge carriers. UV-vis absorption spectra of g-C_3N_4 and Cv-g-C_3N_4 show the difference in absorption edges of the two samples. As seen in Figure 4b, the intrinsic absorption edge of Cv-g-C_3N_4 shows a red shift compared with that of g-C_3N_4. In addition, the absorption spectrum of Cv-g-C_3N_4 extends to the whole visible light region, even in the infrared region, thereby enhancing the absorption of light. This is consistent with the previous reports that vacancy defects can increase the visible light absorption of photocatalysts [33]. From the absorption spectra and simulation results (Figures 4d and 4g, both g-C_3N_4 and Cv-g-C_3N_4 are direct-gap semiconductors), the corresponding band gaps

of g-C_3N_4 and Cv-g-C_3N_4 can be derived as 2.73 and 2.68 eV respectively (Figure 4c), indicating that carbon vacancy could narrow the band gap of g-C_3N_4. Thus, the excitation of valence band electrons in Cv-g-C_3N_4 will be much easier than that in g-C_3N_4. In order to determine the position of the conduction band and the valence band of g-C_3N_4 and Cv-g-C_3N_4, Mott–Schottky measurements were performed. As shown in Figure S4 (In supporting information), both of the two samples displayed n-type semiconductor characteristic. The flat-band potentials of both g-C_3N_4 and Cv-g-C_3N_4 is estimated to be about -1.29 eV versus SCE. For n-type semiconductor, the conduction band position is very close to their flat-band potential. Therefore, the conduction band potentials of both g-C_3N_4 and Cv-g-C_3N_4 is -1.29 eV versus SCE, which more negative than the redox potential of O_2/H_2O_2 (0.695 V). The VB potentials are calculated to be 1.44 and 1.39 eV for g-C_3N_4 and Cv-g-C_3N_4 by using the formula Eg = Ev – Ec (Eg: band gap, Ev: VB potential, Ec: CB potential). This up shift of VB potential may be caused by the valence band broadening which could be attributed to the carbon vacancy.

To further understand the change of the band structure induced by carbon vacancies, the band structures and the electron densities of g-C_3N_4 and Cv-g-C_3N_4 were simulated via the plane-wave-pseudopotential approach based on the density functional theory. From Figures 4d and 4g, it can be seen that the carbon vacancies could narrow the band gap of g-C_3N_4 to enhance its visible light absorption. This parallels the results of UV-vis absorption spectra. Meanwhile, the energy level density of valence band of Cv-g-C_3N_4 is much higher than that of g-C_3N_4, revealing that

carbon vacancies make Cv-g-C_3N_4 instead of g-C_3N_4 possess more excitable electrons. This is understandable after considering that carbon vacancies reduced the symmetry of g-C_3N_4 and produced the effect of electron delocalization. The symmetry reduction and electron delocalization are shown in the electron density maps (Figures 4e and 4f).

Photoluminescence (PL) spectra were used to explore the recombination and separation of photogenerated electrons and holes in the g-C_3N_4 and Cv-g-C_3N_4 samples (Figure 5a). The emission peak appearing at about 455 nm is attributed to the direct electron-hole recombination of band transition. Compare with pure g-C_3N_4, Cv-g-C_3N_4 possess a much weaker emission peak, implying that the separation efficiency of photogenerated carriers is improved by carbon vacancies. The reason of increased separation efficiency can be explained by electrical conductivity. Electrochemical impedance spectroscopy (EIS) was employed to study the electrical conductivity of the resulting samples. Figure S5 (In supporting information) reveals that the Nyquist plots diameter of Cv-g-C_3N_4 is much smaller than that of g-C_3N_4, confirming that the carbon vacancies could increase the electrical conductivity. Carbon vacancies originate from the breaking of the covalent bonds between carbon and nitrogen atoms, accompany by many unsaturated N atoms. These unsaturated N atoms could act as the paramagnetic centers and attract photoelectrons from the conduction band of Cv-g-C_3N_4 (Figure 5b). Therefore, carbon vacancies could significantly inhibit the recombination of photogenerated carriers, thus increasing the yield of photoelectrons.

306 Based on the experimental observations in conjunction with theoretical calculation,
307 the fact that Cv-g-C_3N_4 could produce more photoelectrons can be attributed to the
308 following. First, carbon vacancies made Cv-g-C_3N_4 to hold more excitable electrons;
309 second, carbon vacancies could narrow the band gap of g-C_3N_4 to enhance its visible
310 light absorption; and third, carbon vacancies could significantly inhibit the
311 recombination of photogenerated carriers.

312 Besides the amount of photogenerated electrons, the H_2O_2 production performance
313 may also depend on the adsorption capacity and adsorption strength of molecular
314 oxygen onto the surface of g-C_3N_4 because the photocatalytic process is surface
315 related. In general, adsorption capacity is proportional to the surface area of a sample.
316 The surface areas of g-C_3N_4 and Cv-g-C_3N_4 were analyzed through nitrogen
317 adsorption-desorption isotherms. Figure 6a shows that the Brunauer–Emmett–Teller
318 specific surface areas of g-C_3N_4 and Cv-g-C_3N_4 are 8.8 and 9.4 m^2/g, respectively,
319 indicating that the adsorption amount of molecular oxygen on Cv-g-C_3N_4 is
320 approximate to that on g-C_3N_4.

321 For adsorption strength, it is strongly dependent on the interaction between surface
322 sites and adsorbates, thereby classified into different adsorption types including
323 physisorption and chemisorption. Temperature-programmed desorption (TPD)
324 investigations were carried out to study the adsorption type and adsorption strength of
325 molecular oxygen on the surface of two samples. As shown in Figure 6b (Detailed
326 experiments can be found in supporting information), there are two types of O_2
327 adsorbed species present on Cv-g-C_3N_4 compared to only one on g-C_3N_4. The peak at

about 120 ^{o}C relates to physical adsorption. This peak from Cv-g-C_3N_4 is much weaker than that from g-C_3N_4. Moreover, the peak at 270 ^{o}C, corresponding to the strong chemisorption species of O_2, could be observed for Cv-g-C_3N_4 but not for g-C_3N_4. These observations suggest that, although the amount of molecular oxygen adsorbed on g-C_3N_4 and Cv-g-C_3N_4 is comparable, the adsorption strength of molecular oxygen on Cv-g-C_3N_4 is stronger than that on g-C_3N_4. According to previous reports, the oxygen atom of O_2 has a single electron, making the gas behave as a Lewis acid. Meanwhile, the N atom of amino group around carbon vacancy acts as a Lewis base. These behaviors indicate that O_2 can interact with the N atom of amino group via Lewis acid–base interactions. Therefore, the chemisorption of O_2 over Cv-g-C_3N_4 involves the O atom of O_2 bonding with the N atom of amino group around the carbon vacancy. The stronger the adsorption is, the easier the electrons transfer [34].

In order to explore the correlation between adsorption and electron transfer directly, photocurrent decay measurements were conducted. Under Ar atmosphere, the photocurrent generated on both g-C_3N_4 and Cv-g-C_3N_4 electrode is stabilized with irradiation time during the entire irradiation period (Figure 7a). However, the photocurrent of both g-C_3N_4 and Cv-g-C_3N_4 gradually decay under O_2 atmosphere (Figure 7b). Moreover, the photocurrent decay of g-C_3N_4 is much slower than that of Cv-g-C_3N_4. Since photocurrent decay mainly occurs due to the competition between O_2 and ITO glass for trapped electrons [34], it is concluded that carbon vacancies help the photogenerated electrons to transfer from g-C_3N_4 to the adsorbed O_2.

Chemical adsorption sites are often regarded as reaction centers capable of activating adsorbate [33, 34]. Activation generally refers to the process whereby adsorbate is excited for a subsequent reaction. Therefore, it will be easier to reduce molecular oxygen on Cv-g-C_3N_4 than on g-C_3N_4. To test this hypothesis, linear sweep voltammetry (LSV) was carried out to investigate the reduction of oxygen. Figure 7c shows the ORR catalytic performance for g-C_3N_4 and Cv-g-C_3N_4 under the LSV test. Compare with the LSV curve of g-C_3N_4, cathodic current is enhanced greatly on Cv-g-C_3N_4. This observation proves that carbon vacancies make the molecular oxygen reduction on Cv-g-C_3N_4 easier than that on g-C_3N_4 (Figure 7d).

Hydrogen peroxide might be generated through either a sequential two-step single-electron indirect reduction ($O_2 \rightarrow \cdot O_2^- \rightarrow H_2O_2$) or an one-step two-electron direct reduction ($O_2 \rightarrow H_2O_2$) route (Figure 8a). To clarify the mechanisms of photocatalytic H_2O_2 production on g-C_3N_4 and Cv-g-C_3N_4, DMPO spin-trapping ESR technique was employed to measure the $\cdot O_2^-$ in photocatalysis (Figure 8b). Four characteristic peaks of DMPO-$\cdot O_2^-$ are clearly observed in methanolic suspensions of g-C_3N_4, while no peak could be found in methanolic suspension of Cv-g-C_3N_4. The significant difference in DMPO-$\cdot O_2^-$ signals strongly implies that carbon vacancies change the transfer pathway of photoelectrons. Although Cv-g-C_3N_4 could not produce $\cdot O_2^-$, it could generate H_2O_2 directly under the visible light irradiation. Based on these observations, we speculate that H_2O_2 in g-C_3N_4 suspension is achieved through a two-step single-electron indirect reduction pathway ($e^- \rightarrow \cdot O_2^- \rightarrow H_2O_2$); while in Cv-g-$C_3N_4$ suspension, it is achieved through one-step two-electron direct

372 reduction pathway ($e^- \rightarrow H_2O_2$). To confirm this speculation, active species trapping
373 experiments were further carried out. As shown in Figures 9a and 9b, the addition of
374 p-benzoquinone (PBQ, 1 mM, $\cdot O_2^-$ scavenger) does not change the H_2O_2 generation
375 on Cv-g-C_3N_4 while it could actually depress the H_2O_2 generation on g-C_3N_4. This
376 unambiguously proves that carbon vacancies change the H_2O_2 generation pathway
377 over g-C_3N_4 under visible light from a two-step single-electron indirect reduction to
378 an one-step two-electron direct reduction.

379 The one-step two-electron pathway of H_2O_2 production was further confirmed by
380 the rotating disc electrode (RDE) experiment. For pristine g-C_3N_4, the typical
381 two-step pathway at around -0.5 V and -1.2 V is observed, indicating a successive
382 single-electron reduction (Figure S6, in the supporting information). Interestingly,
383 when g-C_3N_4 is replaced by Cv-g-C_3N_4, the first reduction plateau vanished. The LSV
384 curves show a single-step plateau, indicating an one-step two-electron direct reduction
385 pathway.

386 Zhang and his coworkers have investigated the effects of various nitrogen species
387 in ORR process [35]. They observed that electron transfer number depends on the
388 amino nitrogen components in metal-free catalysts. In our system, carbon vacancies
389 are surrounded by many N-dangling bands (unsaturated N atoms). Dangling bonds of
390 N atoms are compensated by adsorbed hydrogen and form many amino groups. The
391 formation of amino group on Cv-g-C_3N_4 is confirmed by FTIR measurements (Figure
392 10a). Therefore, the one-step two-electron reduction pathway could be attributed to
393 amino groups around carbon vacancies. To clarify this point, it is necessary to remove

amino groups from Cv-g-C_3N_4 and then compare the H_2O_2 production performance before and after deamination. In this work, a simple and common chemical deamination approach was designed to remove the amino groups from Cv-g-C_3N_4 (Detailed experiments can be found in supporting information). As seen from Figure 10b that, after deamination, the absorption band of amino group is significantly decreased. This result suggests that amino groups are effectively removed in deamination approach. Furthermore, H_2O_2 and $\cdot O_2^-$ measurements were carried out to evaluate the contribution of amino group to H_2O_2 production. As shown in Figure 11a, the deamination could greatly inhibit the generation of H_2O_2 in Cv-g-C_3N_4, while the ratio of maximum concentration of hydrogen peroxide after the deamination is only about 19.9% of that before the deamination. Moreover, it is very interesting to notice that deamidated Cv-g-C_3N_4 in methanol dispersion gives stronger ESR signals of DMPO-$\cdot O_2^-$ (Figure 11b). However, these generated superoxide radicals could not be produced before deamination, confirming that one-step two-electron direct reduction pathway is attributed to amino groups around carbon vacancies.

The stability of the Cv-g-C_3N_4 during the photocatalytic H_2O_2 production was evaluated by recycling test (Figure S7, in the supporting Information). No significant change in the photocatalytic activity occurs after four cycles, indicating that Cv-g-C_3N_4 is stable during the photocatalytic H_2O_2 production.

4. Conclusions

In summary, we have demonstrated that carbon vacancies could be introduced on the

surface of g-C_3N_4 by simple calcinations with argon gas. The carbon vacancies modified g-C_3N_4 could efficiently reduce atmospheric O_2 to H_2O_2 under visible light, without using any precious metal cocatalysts or organic scavengers. The presence of carbon vacancies could reduce the symmetry of g-C_3N_4 and narrow down its band gap, thus extending the visible light absorption and increasing the excitable electrons. Moreover, carbon vacancies could activate O_2 and change the H_2O_2 generation pathway from a two-step single-electron indirect reduction to a one-step two-electron direct reduction. This study not only provides a new strategy to improve the photocatalytic H_2O_2 production, but also underlines the significance of the correlation between the surface defect structure and the activity of semiconductor photocatalysts.

Acknowledgment

This work was supported by National Science Foundation of China (Grants 21473248), scientific research start-up funds for postdoctor (Y55P411601), the "Western Light" Program of Chinese Academy of Sciences (2015-XBQN-B-06) and the CAS/SAFEA International Partnership Program for Creative Research Teams. We gratefully acknowledge Dr Tao Pang (AQNU, China) for valuable discussions and Prof. Y. S. Chai for language polish.

Reference

[1] J. M. Campos-Martin, G. Blanco-Brieva, J. L. Fierro, Angew. Chem. Int. Ed. 45 (2006) 6962-6984.

[2] J. J. Peng, F. Shi, Y. L. Gu, Y. Q. Deng, Green Chem., 5 (2003) 224-226.

[3] S. Niwa, M. Eswaramoorthy, J. Nair, A. Raj, N. Itoh, H. Shoji, T. Namba, F. Mizukami, Science 295 (2002) 105-107.

[4] Z. H. Ai, L. R. Lu, J. P. Li, L. Z. Zhang, J. R. Qiu, M. H. Wu, J. Phys. Chem. C, 117 (**2007**) 4087-4093.

[5] Y. j. Cui, Z. X. Ding, P. Liu, M. Antouietti, X. Z. Fu, X. C. Wang, Phys. Chem. Chem. Phys., 14 (2012) 1455-1462.

[6] Y. X. Qin, F. H. Song, Z. H. Ai, P. P. Zhang, L. Z. Zhang, Environ. Sci. Technol. 49 (2015) 7948-7956.

[7] R. Hage, A. Lienke, Angew. Chem. Int. Ed. 45 (2006) 206-222.

[8] C. Prat, M. Vicente, S. Esplugas. Water Res. 22 (1988) 663-668.

[9] M. Perez, F. Torrades, X. Domenech, J. Peral, Water Res. 36 (2002) 2703-2710.

[10] X. F. Chen, J. S. Zhang, X. Z. Fu, M. Antonietti, X. C. Wang, J. Am. Chem. Soc. 131 (2009) 11658-11659.

[11] V. R. Choudhary, A. G. Gaikwad, S. D. Sansare, Angew. Chem. Int. Ed. 40 (2001) 1776-1779.

[12] P. Landon, P. J. Collier, A. J. Papworth, C. J. Kiely, G. J. Hutchings, Chem. Commun. 2002 2058-2059.

[13] T. P. Fellinger, F. Hasché, P. Strasser, M. Antonietti, J. Am. Chem. Soc. 134 (2012) 4072-4075.

[14] V. Maurino, C. Minero, G. Mariella, E. Pelizzetti, Chem. Commun. 2005 2627-2629.

463 [15] V. Diesen, M. Jonsson, J. Phys. Chem. C, 118 (2014) 10083-10087.
464 [16] D. Tskamoto, A. Shiro, Y. Shiraishi, Y. Sugano, S. Ichikawa, S. Tanaka, T. Hirai,
465 ACS Catal. 2 (2012) 599-603.
466 [17] X. J. Ye, Y. J. Cui, X. Q. Qiu, X. C. Wang, Appl. Catal., B Environ. 152-153
467 (2014) 383-389.
468 [18] D. F. Wang, T. Kako, J. H. Ye, J. Am. Chem. Soc. 130 (2008) 2724-2725.
469 [19] X. C. Wang, K. Maeda, A. Thomas, K. Takanabe, G. Xin, J. M. Carlsson, K.
470 Domen, M. Antonietti, Nat. Mater. 8 (2009) 76-80.
471 [20] X. C. Wang, K. Maeda, X. F. Chen, K. Takanabe, K. Domen, Y. D. Hou, X. Z. Fu,
472 M. Antonietti, J. Am. Chem. Soc. 131 (2009) 1680-1681.
473 [21] F. Z. Su, S. C. Mathew, G. Lipner, X. Z. Fu, M. Antonietti, S. Blechert, X. C.
474 Wang, J. Am. Chem. Soc. 132 (2010) 16299-16301.
475 [22] G. H. Dong, L. Z. Zhang, J. Phys. Chem. C, 117 (2013) 4062-4068.
476 [23] G. H. Dong, Z. H. Ai, L. Z. Zhang, Water Res. 66 (2014) 22-30.
477 [24] Y. Shiraishi, S. Kanazama, Y. Kofuji, H. Sakamoto, S. Ichikawa, S. Tanaka, T.
478 Hirai, Angew. Chem. Int. Ed. 53 (2014) 13454-13459.
479 [25] S. C. Yan, Z. S. Li, Z. G. Zou, Langmuir 26 (2010) 3894-3910.
480 [26] S. C. Yan, Z. S. Li, Z. G. Zou, Langmuir, 25 (2009) 10397-10401.
481 [27] G. H. Dong, W. K. Ho, Y. H. Li, L. Z. Zhang, Appl. Catal., B Environ. 174
482 (2015) 477-485.
483 [28] Q. J. Xiang, J. G. Yu, M. Jaroniec, J. Phys. Chem. C, 115 (2011) 7355-7363.
484 [29] J. G. Yu, K. Wang, W. Xiao, B. Cheng, Phys. Chem. Chem. Phys., 16 (2014)
485 11492-11501.
486 [30] A. L. Linsebigler, G. Q. Lu, J. T. Yates, Chem. Rev. 95 (1995) 735-758.
487 [31] Y. H. Lv, Y. F. Liu, Y. Y. Zhu, Y. F. Zhu. J. Mater. Chem. A, 2 (2014)

1174-1182.

[32] D. M. Chen, Z. H. Wang, T. Z. Ren, D. Hao, W. Q. Yao, R. L. Zong, Y. F. Zhu, J. Phys. Chem. C, 118 (2014) 15300-15307.

[33] H. Li, J. Shang, Z. H. Ai and L. Z. Zhang, J. Am. Chem. Soc., 137 (2015) 6393-6399.

[34] G. H. Dong, W. K. Ho, C. Y. Wang, J. Mater. Chem. A**,** 3 (2015) 23435-23441.

[35] C. Z. Zhang, R. Hao, H. B. Liao, Y. L. Hou, Nano Energy, 2 (2013) 88-97.

[36] G. H. Dong, Z. H. Ai, L. Z. Zhang, RSC Adv., 4 (2014) 5553-5560.

[37] L. Wang, M. H. Cao, Z. H. Ai, L. Z. Zhang, Environ. Sci. Technol. 48 (2014), 3354-3362.

[38] P. Niu, L. C. Yin, Y. Q. Yang, G. Liu, H. M. Cheng, Adv. Mater. 26 (2014), 8046-8052.

Figure Captions

Scheme 1. (a) Schematic of g-C_3N_4; (b) carbon vacancy and amino group in g-C_3N_4.

Figure 1. (a) XRD patterns of g-C_3N_4 and Cv-g-C_3N_4; (b) C/N molar ratio in the g-C_3N_4 and Cv-g-C_3N_4.

Figure 2. (a) high-resolution XPS spectra of C 1s of g-C_3N_4 and Cv-g-C_3N_4; (b) high-resolution XPS spectra of N 1s of g-C_3N_4 and Cv-g-C_3N_4; (c) ESR spectra of g-C_3N_4 and Cv-g-C_3N_4; (d) possible formation mechanism of carbon vacancy.

Figure 3. (a) The concentration of generated H_2O_2 in different g-C_3N_4 systems; (b) The concentration of generated H_2O_2 in different Cv-g-C_3N_4 systems; (c) H_2O_2 production is accomplished by photocatalysis; (d) the concentration of H_2O_2 generated in g-C_3N_4 and Cv-g-C_3N_4 systems.

Figure 4. (a) The photocurrent generated on g-C_3N_4 and Cv-g-C_3N_4; (b) UV-vis diffuse reflectance spectra of g-C_3N_4 and Cv-g-C_3N_4; (c) plots of $(ahv)^2$ vs the energy of absorbed light of g-C_3N_4 and Cv-g-C_3N_4; (d) calculated band structure of g-C_3N_4; (e) calculated electron density of g-C_3N_4; (f) calculated electron density of Cv-g-C_3N_4; (g) calculated band structure of g-C_3N_4.

Figure 5. (a) photoluminescence (PL) spectra of g-C_3N_4 and Cv-g-C_3N_4; (b) carbon vacancy could significantly inhibit the recombination of photogenerated carriers.

Figure 6. (a) N_2 adsorption-desorption isotherms of g-C_3N_4 and Cv-g-C_3N_4; (b) TPD spectra of g-C_3N_4 and Cv-g-C_3N_4.

Figure 7. (a) Photocurrent decay measurements were conducted under Ar atmosphere; (b) Photocurrent decay measurements were conducted under O_2 atmosphere; (c) linear

sweep voltammetry (LSV) curves of g-C_3N_4 and Cv-g-C_3N_4; (d) carbon vacancy makes the molecular oxygen reduction on Cv-g-C_3N_4 easier than that on g-C_3N_4.

Figure 8. (a) The possible generation routes of H_2O_2; (b) 5,5-dimethyl-pyrroline N-oxide (DMPO) spin trapping ESR technique to measure $\cdot O_2^-$ generated during the generation of H_2O_2.

Figure 9. (a) The influence of p-benzoquinone (PBQ, 1 mM, $\cdot O_2^-$ scavenger) for the H_2O_2 generation on g-C_3N_4; (b) the influence of p-benzoquinone (PBQ, 1 mM, $\cdot O_2^-$ scavenger) for the H_2O_2 generation on Cv-g-C_3N_4.

Figure 10. (a) FT-IR spectra of g-C_3N_4 and Cv-g-C_3N_4 samples; (b) FT-IR spectra of Cv-g-C_3N_4 before and after the deamination.

Figure 11. (a) The influence of deamination for the H_2O_2 generation on Cv-g-C_3N_4; (b) the influence of deamination for the $\cdot O_2^-$ generation; (c) amino group changed the H_2O_2 generation pathway from single-electron reduction to two-electron reduction.

Figure Captions

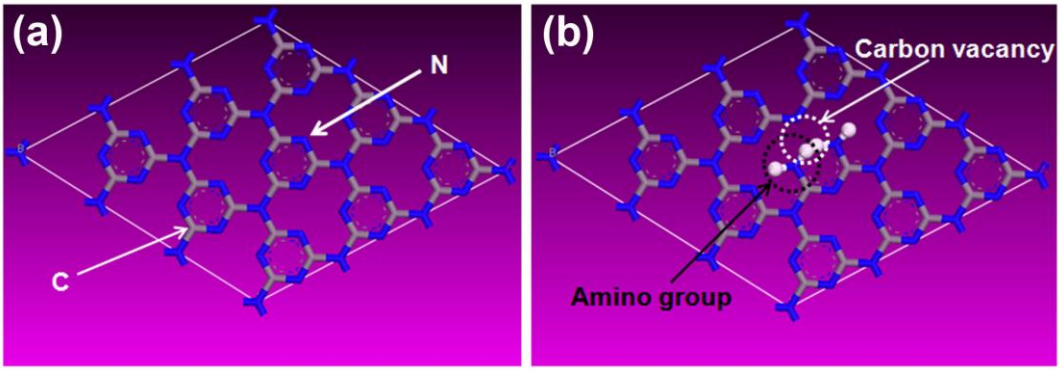

Scheme 1. (a) Schematic of g-C_3N_4; (b) carbon vacancy and amino group in g-C_3N_4.

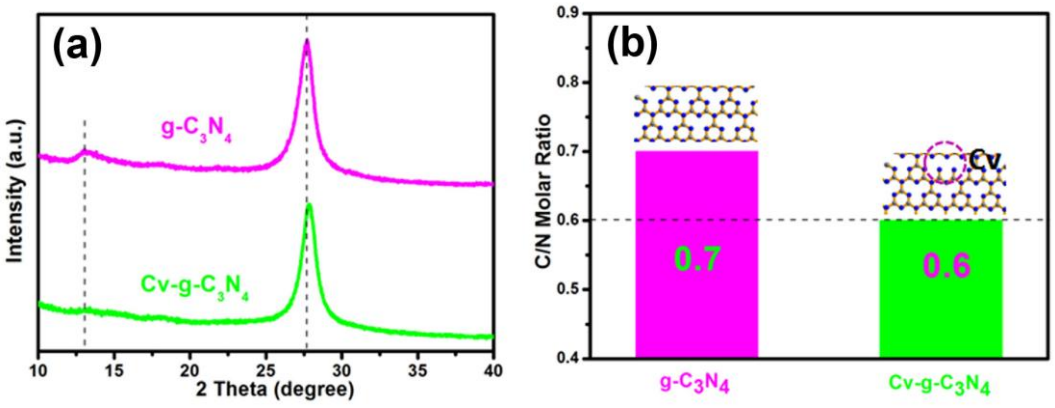

Figure 1. (a) XRD patterns of g-C_3N_4 and Cv-g-C_3N_4; (b) C/N molar ratio in the g-C_3N_4 and Cv-g-C_3N_4.

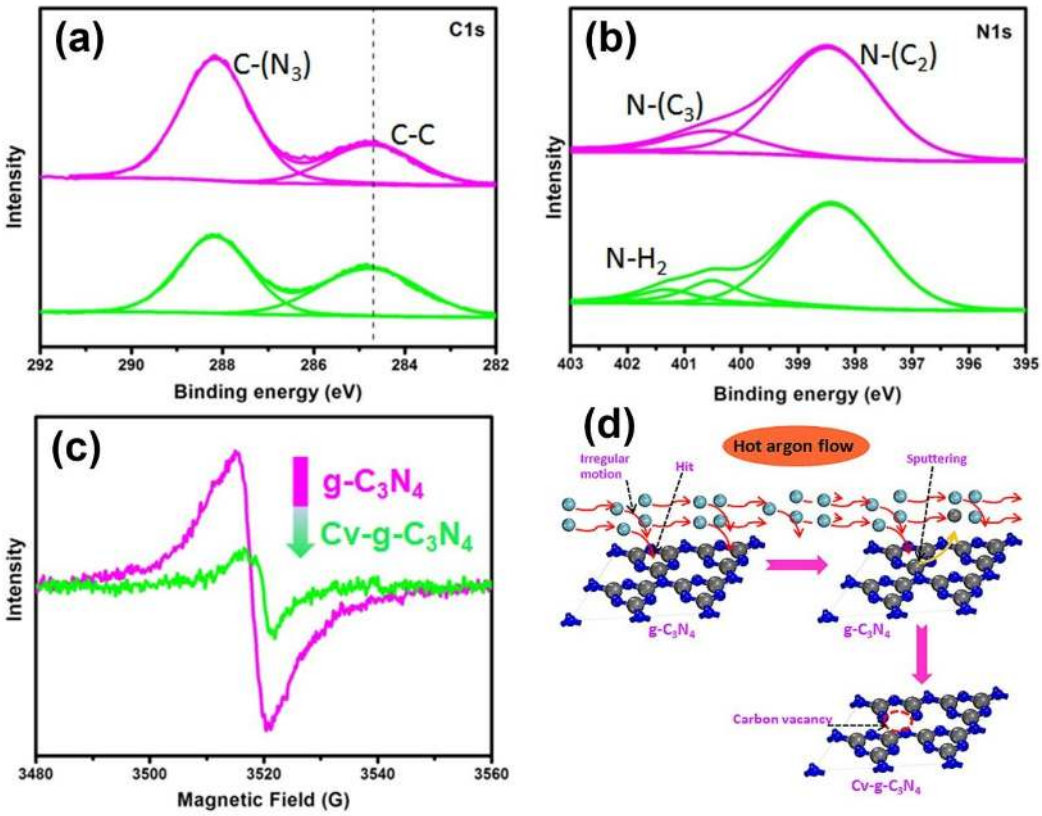

555

556 **Figure 2.** (a) High-resolution XPS spectra of C 1s of g-C_3N_4 and Cv-g-C_3N_4; (b)

557 high-resolution XPS spectra of N 1s of g-C_3N_4 and Cv-g-C_3N_4; (c) ESR spectra of

558 g-C_3N_4 and Cv-g-C_3N_4; (d) possible formation mechanism of carbon vacancy.

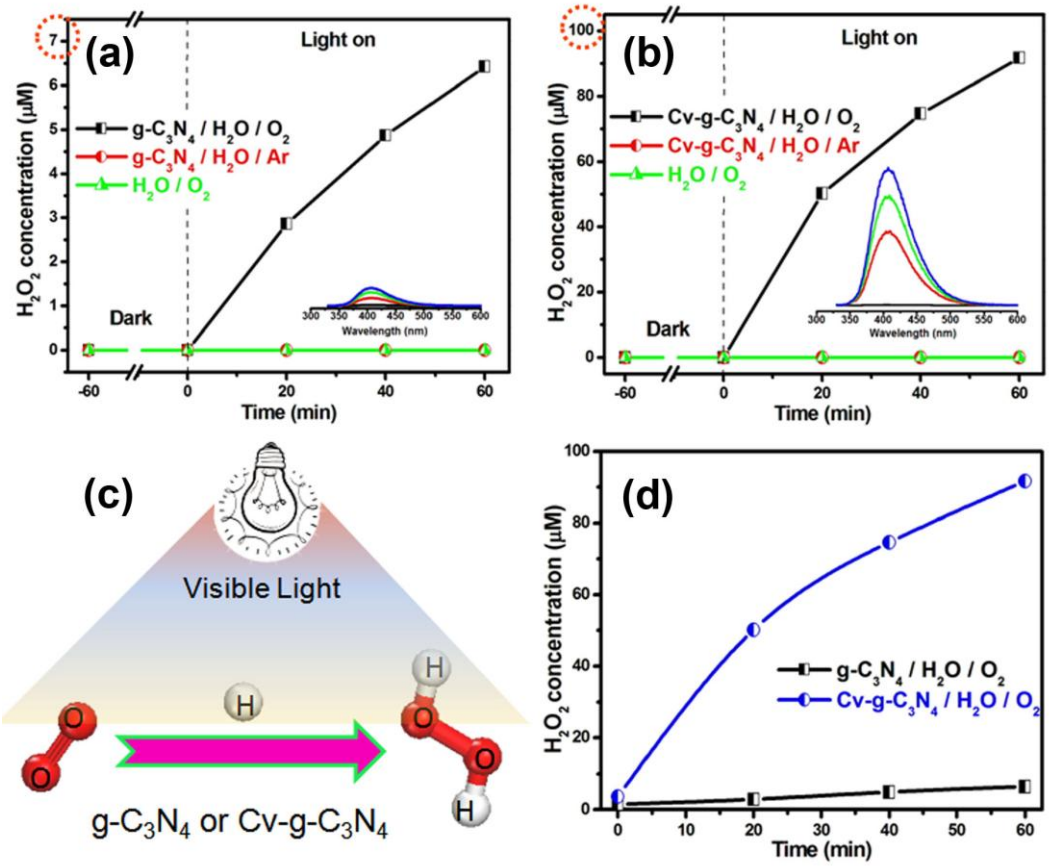

559

560 **Figure 3.** (a) The concentration of generated H_2O_2 in different g-C_3N_4 systems; (b)

561 The concentration of generated H_2O_2 in different Cv-g-C_3N_4 systems; (c) H_2O_2

562 production is accomplished by photocatalysis; (d) the concentration of H_2O_2

563 generated in g-C_3N_4 and Cv-g-C_3N_4 systems.

564

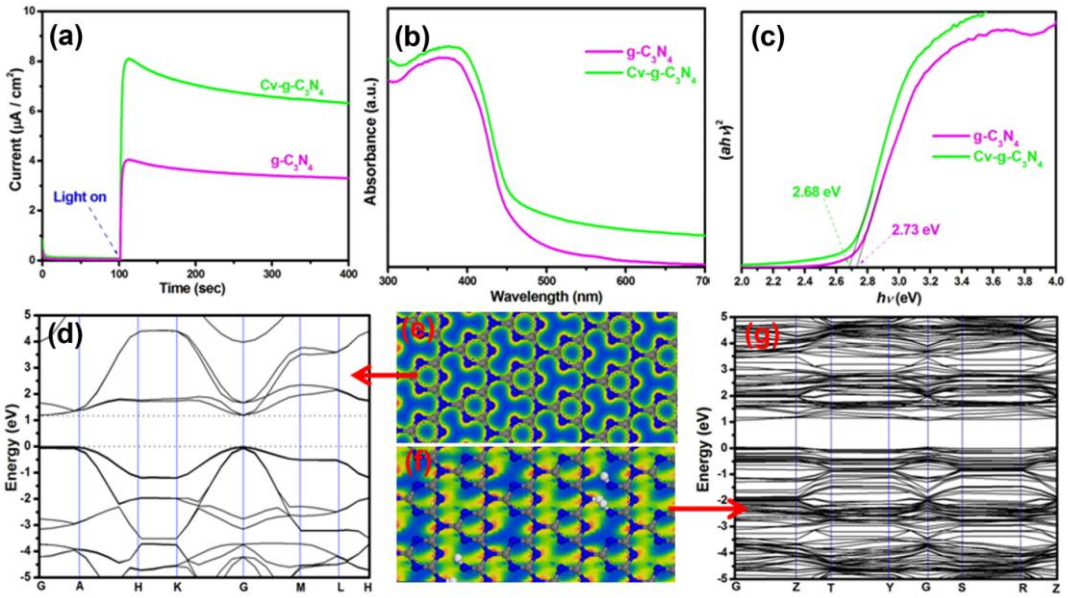

565

566 **Figure 4.** (a) The photocurrent generated on g-C_3N_4 and Cv-g-C_3N_4; (b) UV-vis

567 diffuse reflectance spectra of g-C_3N_4 and Cv-g-C_3N_4; (c) plots of $(ahv)^2$ vs the energy

568 of absorbed light of g-C_3N_4 and Cv-g-C_3N_4; (d) calculated band structure of g-C_3N_4;

569 (e) calculated electron density of g-C_3N_4; (f) calculated electron density of Cv-g-C_3N_4;

570 (g) calculated band structure of g-C_3N_4.

571

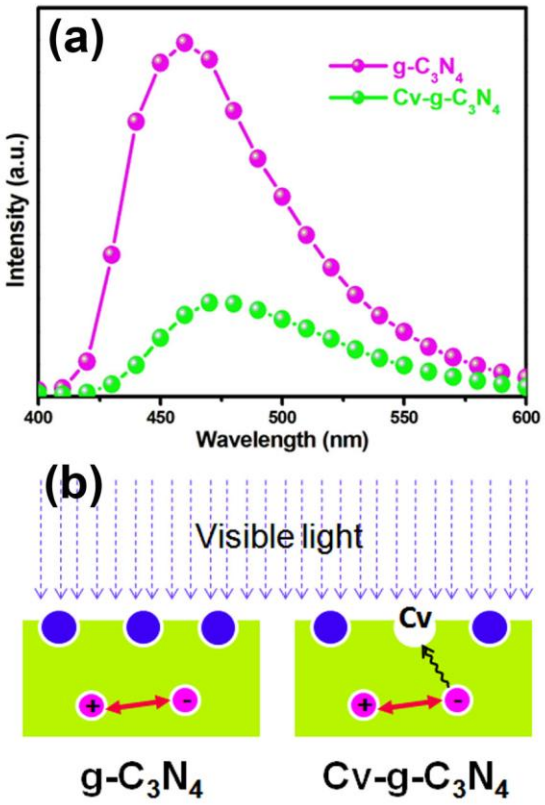

572

573 **Figure 5.** (a) photoluminescence (PL) spectra of g-C_3N_4 and Cv-g-C_3N_4; (b) carbon

574 vacancy could significantly inhibit the recombination of photogenerated carriers.

575

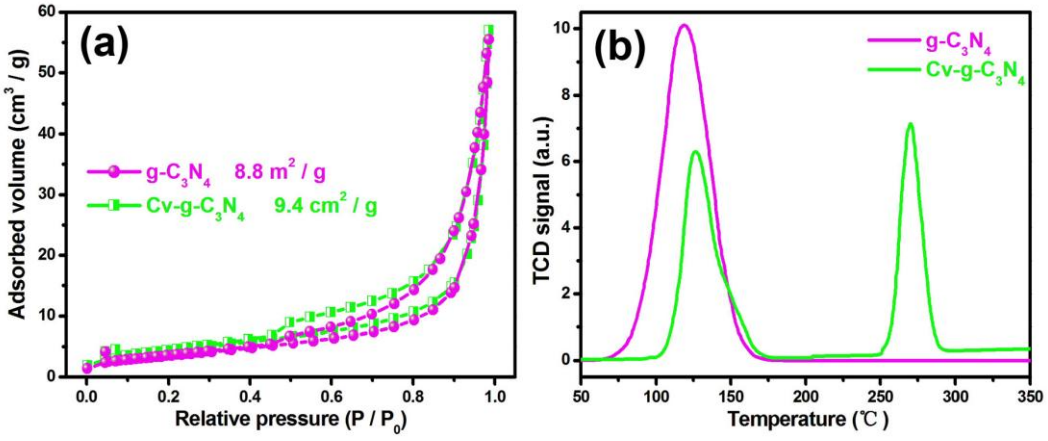

576

577 **Figure 6.** (a) N_2 adsorption-desorption isotherms of g-C_3N_4 and Cv-g-C_3N_4; (b) TPD

578 spectra of g-C_3N_4 and Cv-g-C_3N_4.

579

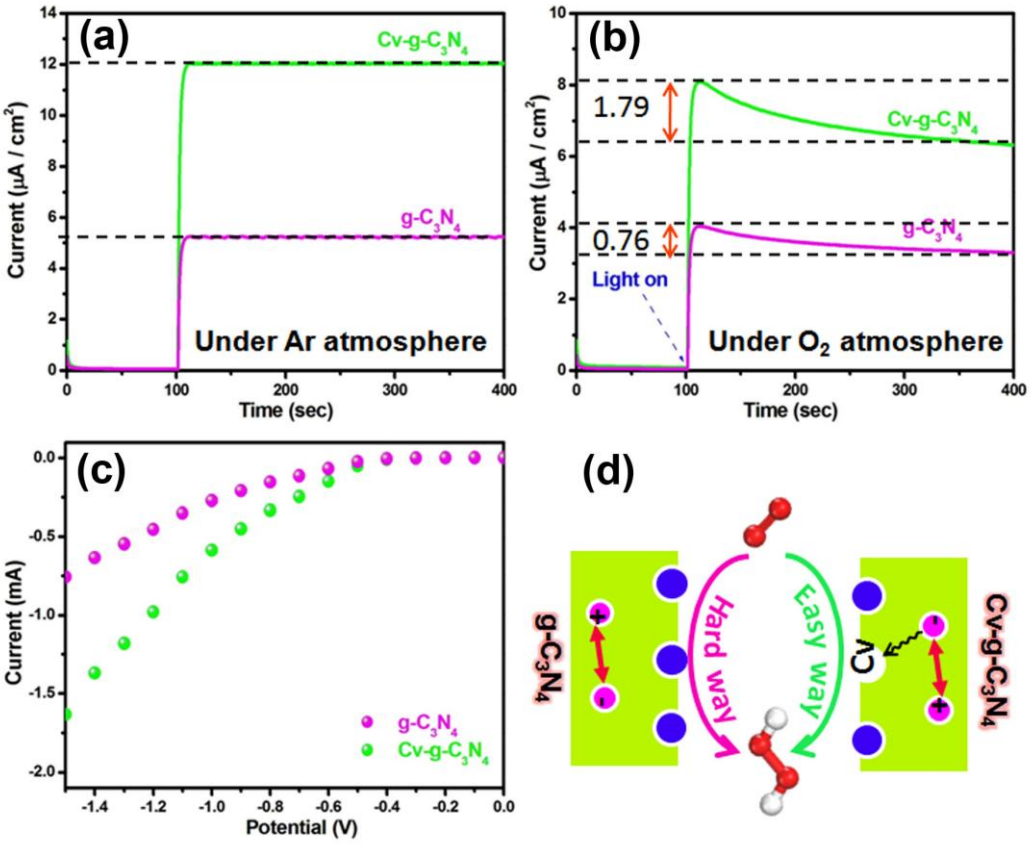

580

581 **Figure 7.** (a) Photocurrent decay measurements were conducted under Ar atmosphere;

582 (b) Photocurrent decay measurements were conducted under O_2 atmosphere; (c) linear

583 sweep voltammetry (LSV) curves of g-C_3N_4 and Cv-g-C_3N_4; (d) carbon vacancy

584 makes the molecular oxygen reduction on Cv-g-C_3N_4 easier than that on g-C_3N_4.

585

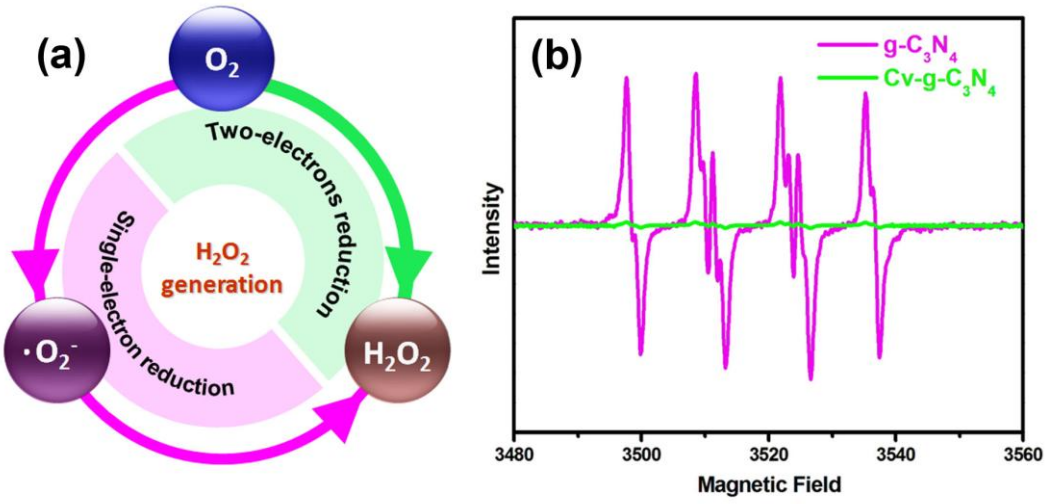

586

Figure 8. (a) The possible generation routes of H_2O_2; (b) 5,5-dimethyl-pyrroline N-oxide (DMPO) spin trapping ESR technique to measure $\cdot O_2^-$ generated during the generation of H_2O_2.

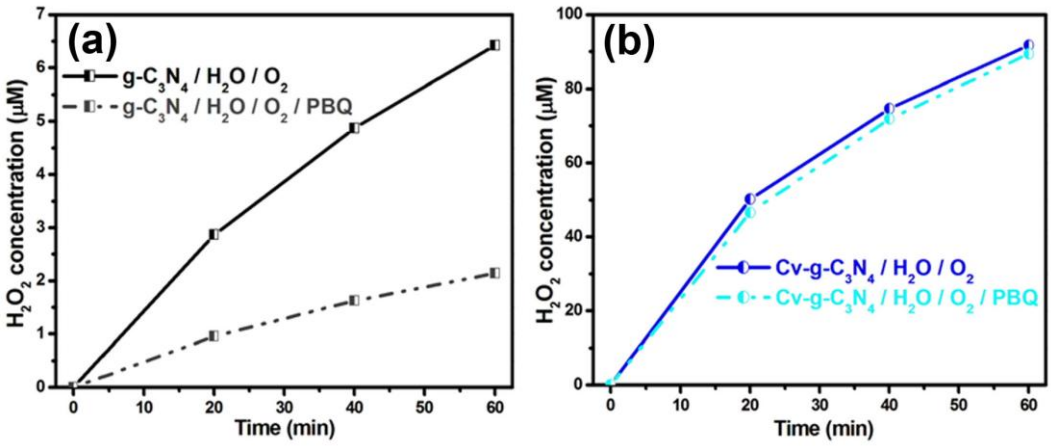

Figure 9. (a) The influence of p-benzoquinone (PBQ, 1 mM, $\cdot O_2^-$ scavenger) for the H_2O_2 generation on g-C_3N_4; (b) the influence of p-benzoquinone (PBQ, 1 mM, $\cdot O_2^-$ scavenger) for the H_2O_2 generation on Cv-g-C_3N_4.

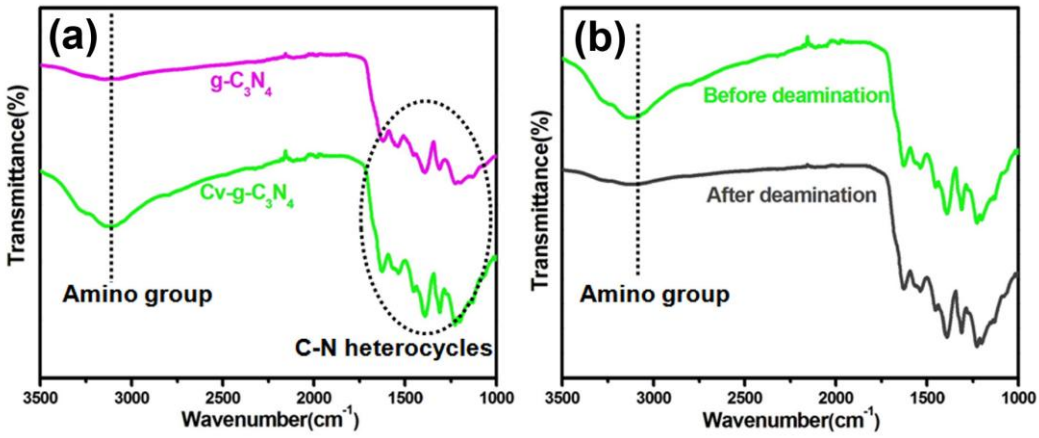

Figure 10. (a) FT-IR spectra of g-C_3N_4 and Cv-g-C_3N_4 samples; (b) FT-IR spectra of Cv-g-C_3N_4 before and after the deamination.

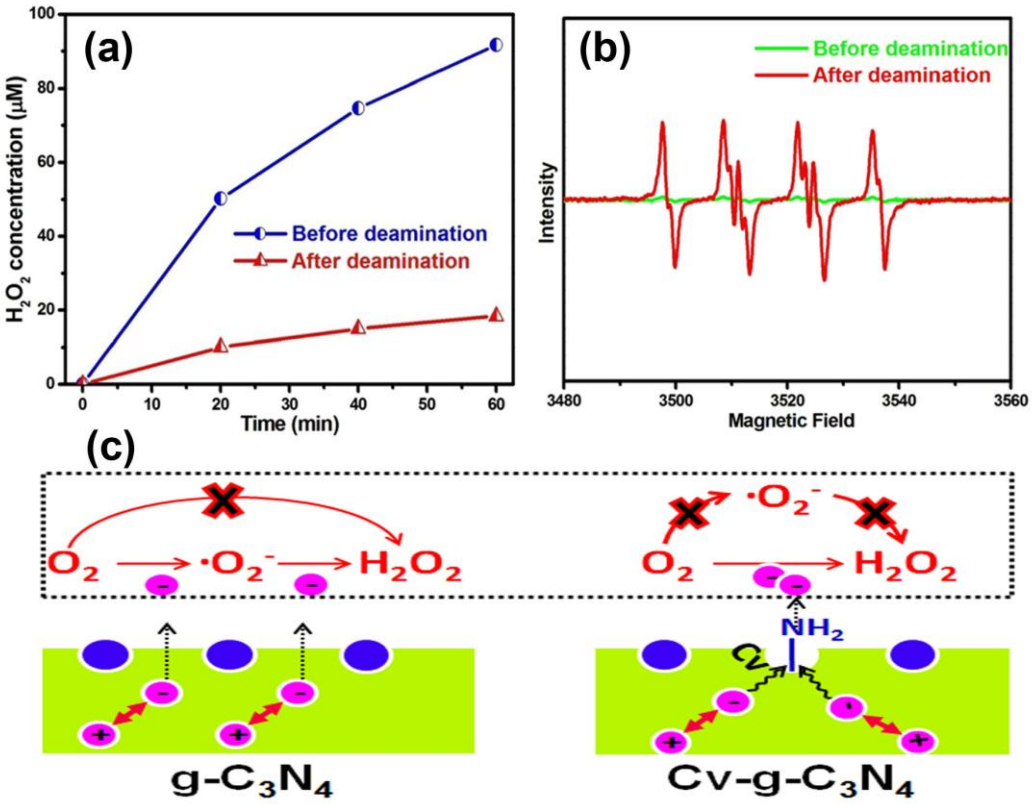

599

600 **Figure 11.** (a) The influence of deamination for the H_2O_2 generation on Cv-g-C_3N_4; (b)

601 the influence of deamination for the $\cdot O_2^-$ generation; (c) amino group changed the H_2O_2

602 generation pathway from single-electron reduction to two-electron reduction.

603

604

605

606 **TOC Brief:** We demonstrated that photocatalytic H_2O_2 production on g-C_3N_4 could
607 be improved by as much as 14 times in the absence of organic scavenger through a
608 carbon vacancy-based strategy. The presence of carbon vacancies changed the H_2O_2
609 generation pathway from a two-step single-electron indirect reduction to an one-step
610 two-electron direct reduction.

611

612 **TOC Art Figure**

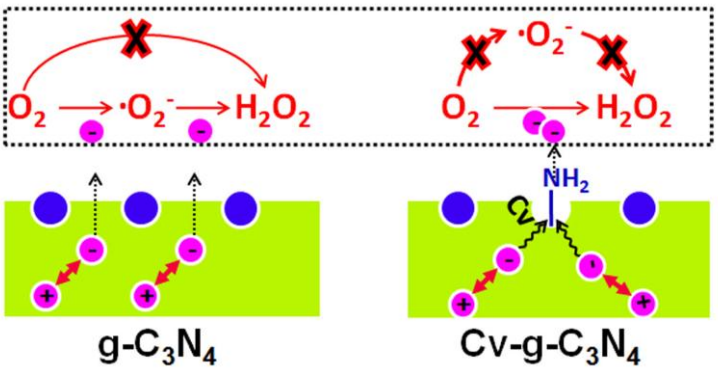

613

614